AGU PUBLICATIONS

Geophysical Research Letters

RESEARCH LETTER
10.1002/2015GL063989

Key Point:
- D″ discontinuity beneath North Atlantic is detected with 304 km average thickness
- D″ discontinuity is not laterally continuous in the region
- Discontinuity termination may be due to the eastern edge of the Farallon plate

Supporting Information:
- Figures S1–S13 and Tables S1 and S2

Correspondence to:
Y. Yao,
yao.yao@utah.edu

Citation:
Yao, Y., S. Whittaker, and M. S. Thorne (2015), D″ discontinuity structure beneath the North Atlantic from *Scd* observations, *Geophys. Res. Lett.*, *42*, doi:10.1002/2015GL063989.

Received 27 MAR 2015
Accepted 30 APR 2015
Accepted article online 5 MAY 2015

D″ discontinuity structure beneath the North Atlantic from *Scd* observations

Yao Yao[1], Stefanie Whittaker[2], and Michael S. Thorne[1]

[1]Department of Geology and Geophysics, University of Utah, Salt Lake City, Utah, USA, [2]Department of Geosciences, University of Alaska Fairbanks, Fairbanks, Alaska, USA

Abstract We analyzed transverse and radial component recordings from the 2010 *M*6.3 southern Spain earthquake (depth = 620 km) recorded on 370 broadband stations in North America. We grouped these seismograms into subarrays and applied fourth root vespa processing (vespagram analysis) in order to enhance low-amplitude arrivals. These vespagrams show clear *Scd* arrivals which indicate the existence of the D″ discontinuity beneath the North Atlantic Ocean (45–60°N, 45–55°W). These observations are best fit with a +2–4% velocity increase at the top of the D″ discontinuity at a height above the core-mantle boundary of 304 ± 14 km. We do not observe *Scd* arrivals at the eastern end of our study region which is consistent with the presence of the easternmost edge of the ancient Farallon plate.

1. Introduction

The D″ discontinuity is a sharp change in *P* and *S* wave velocity of roughly −3 to +3% and +1 to +3%, respectively, ranging from about 100–400 km above the core-mantle boundary (CMB). A phase transition from perovskite (pv) to post-perovskite (ppv) at pressures and temperatures where the discontinuity is observed is a leading candidate for its origin [e.g., *Murakami et al.*, 2004; *Oganov and Ono*, 2004]. Nonetheless, some observations of the discontinuity are difficult to reconcile with a simple phase transition; a situation that is further complicated by lateral variations in lower mantle composition [see *Cobden and Thomas*, 2013, for a review]. In order to understand the origins of the D″ discontinuity, it is important to understand where it exists and what its physical properties are.

Only a handful of observations have been made beneath the North Atlantic (Figure 1a). *Weber and Körnig* [1992] first suggested the possibility of a lower mantle reflector beneath the North Atlantic ridge (labeled 1 in Figure 1a) with a height above the CMB of roughly 200 to 250 km by identifying secondary arrivals between *P* and *PcP*. Several additional studies have provided evidence for D″ discontinuity structure with *P* waves (*Houard and Nataf* [1992], *Krüger et al.* [1995], *Braña and Helffrich* [2004], labeled 2, 4, and 5, respectively, in Figure 1a). Evidence for an *S* wave discontinuity was first demonstrated by *Kendall and Shearer* [1994]. They estimated a D″ height of 250 km above the CMB (labeled 3 in Figure 1a), yet their study was limited to a relatively small number (<10) of seismograms. More recently, *Wallace and Thomas* [2005] showed a laterally varying D″ discontinuity associated with a 1–3% *S* wave velocity increase with heights ranging from 86 to 286 km above the CMB (labeled 6 in Figure 1a). However, this study did not unambiguously confirm the existence of triplicated *S* wave arrivals.

In this paper, we investigate the D″ discontinuity beneath the North Atlantic Ocean using *S* wave observations from the 2010 *M*6.3 southern Spain earthquake recorded on broadband stations in North America. We use a significantly larger data set (370 seismograms for which we use both radial and transverse components) than used in previous studies, which allows us to sort our records into virtual arrays and apply array processing approaches to search for triplicated seismic arrivals in both transverse and radial component recordings. We demonstrate the existence of the discontinuity in a region of the North Atlantic (45–60°N, 45–55°W) that has not previously been investigated.

2. Data and Methods

We investigate D″ discontinuity structure by searching for the *Scd* seismic phase on both transverse and radial component data. *Scd* is a part of the triplication that occurs as the down-going *S* wave refracts below the D″ discontinuity (Figures 2a and 2b). Example synthetic seismograms for transverse and radial components are

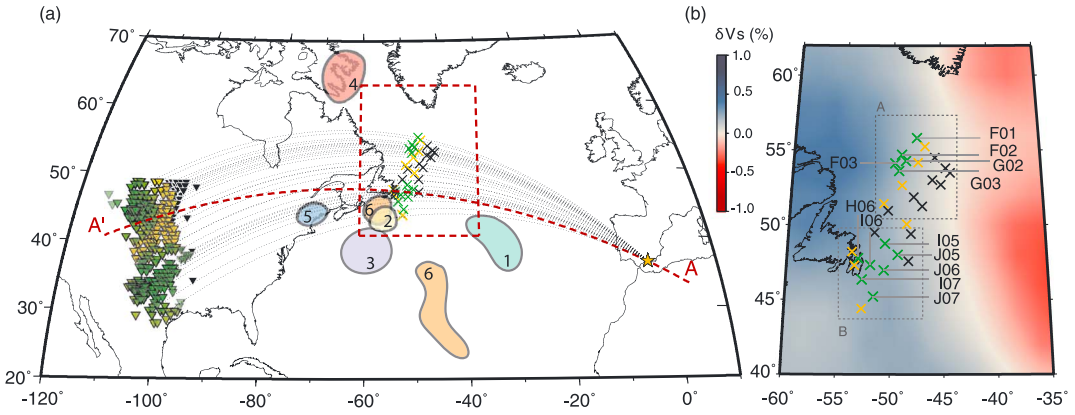

Figure 1. (a) Summary of previous studies of D″ discontinuity structure beneath the North Atlantic. Previous studies are 1, *Weber and Körnig* [1992]; 2, *Houard and Nataf* [1992]; 3, *Kendall and Shearer* [1994]; 4, *Krüger et al.* [1995]; 5, *Braña and Helffrich* [2004]; 6, *Wallace and Thomas* [2005]. The event and stations used in our study are shown as a yellow star and inverted riangles, respectively. The theoretical bounce points of *ScS* on the CMB as calculated by Taup [*Crotwell et al.,* 1999] are shown as green crosses (good cases), yellow crosses (borderline cases), and black crosses (no *Scd* arrival). (b) Detailed view with labeled bins and two clusters of our study area displayed on top of the *S* wave tomography model TXBW [*Grand*, 2002] at the CMB.

shown in Figures 2e and 2f, respectively. These synthetics were computed for a 620 km deep source and a D″ discontinuity model with a 2% increase in *S* wave velocity 250 km above the CMB. There is no change in density; and for radial component synthetics, we included an additional 1% increase in *P* wave velocity. On the transverse component (Figure 2e) *Scd* is observed as a low-amplitude, positive polarity arrival, between the *S* and *ScS* phases. The *Scd*/*S* amplitude ratio increases with increasing epicentral distance. On the radial component (Figure 2f), the *Scd* phase may be obscured by the *SKS* arrival and possibly the *SP* arrival (Figure 2b) at the shortest epicentral distances.

We searched for earthquakes in the European region between January 2005 and June 2014 with M_W between 5.5 and 7.5, event depths greater than 75 km, and recorded at broadband stations in North America within an epicentral distance window of 55° to 90°. For each record, we removed the mean and trend, deconvolved the instrument response, and band-pass filtered the traces from 0.05 to 1 Hz. A total of five earthquakes with 2077 seismograms were originally collected. We inspected each transverse component trace manually and removed traces without clear *S* and *ScS* arrivals. This quality control step cuts our data set down to four events with 833 seismograms.

For each event, we grouped our data into 3° radius geographic bins based on receiver location in order to apply array processing techniques on each subgroup of data. We restricted our bins to just those that contained a minimum of 10 traces, then aligned and normalized each trace to unity on the *S* wave arrival. We applied fourth root vespa processing [*Rost and Thomas*, 2009] on each subarray. Example vespagrams with labeled seismic phases for transverse and radial component synthetic seismograms are shown in Figures 2c and 2d, respectively. On the transverse component, the *Scd* arrival is readily observed with a slowness and travel time in between *S* and *ScS*. On the radial component, the *Scd* arrival is weaker in amplitude than on the transverse component and may potentially be obscured by the *SKS* arrival. Although, *SKS* arrives at a smaller slowness than *Scd*, the slowness resolution of real data is often much poorer than shown for synthetic seismograms. We next screened vespagrams based on signal-to-noise ratio and slowness resolution of *S* and *ScS*. If the *S* and *ScS* arrivals are clearly present in the vespagram with significantly larger amplitude than the background noise, and the energy of the *S* and *ScS* arrivals are relatively concentrated (the slowness resolution is less than 5 s/°), we retain the vespagram. Among these vespagrams, we ultimately discarded the vespagrams for three of the events because either the event was too shallow and the *sS* arrival obscured potential *Scd* arrivals or the *S* and *ScS* arrivals were too close together to unambiguously observe an *Scd* arrival. Only vespagrams from the 620 km deep *M*6.3 southern Spain event of 11 April 2010 were retained for further analysis. Our final data set consisted of 370 seismograms and 31 vespagrams (recorded on each component). In each vespagram we searched for the

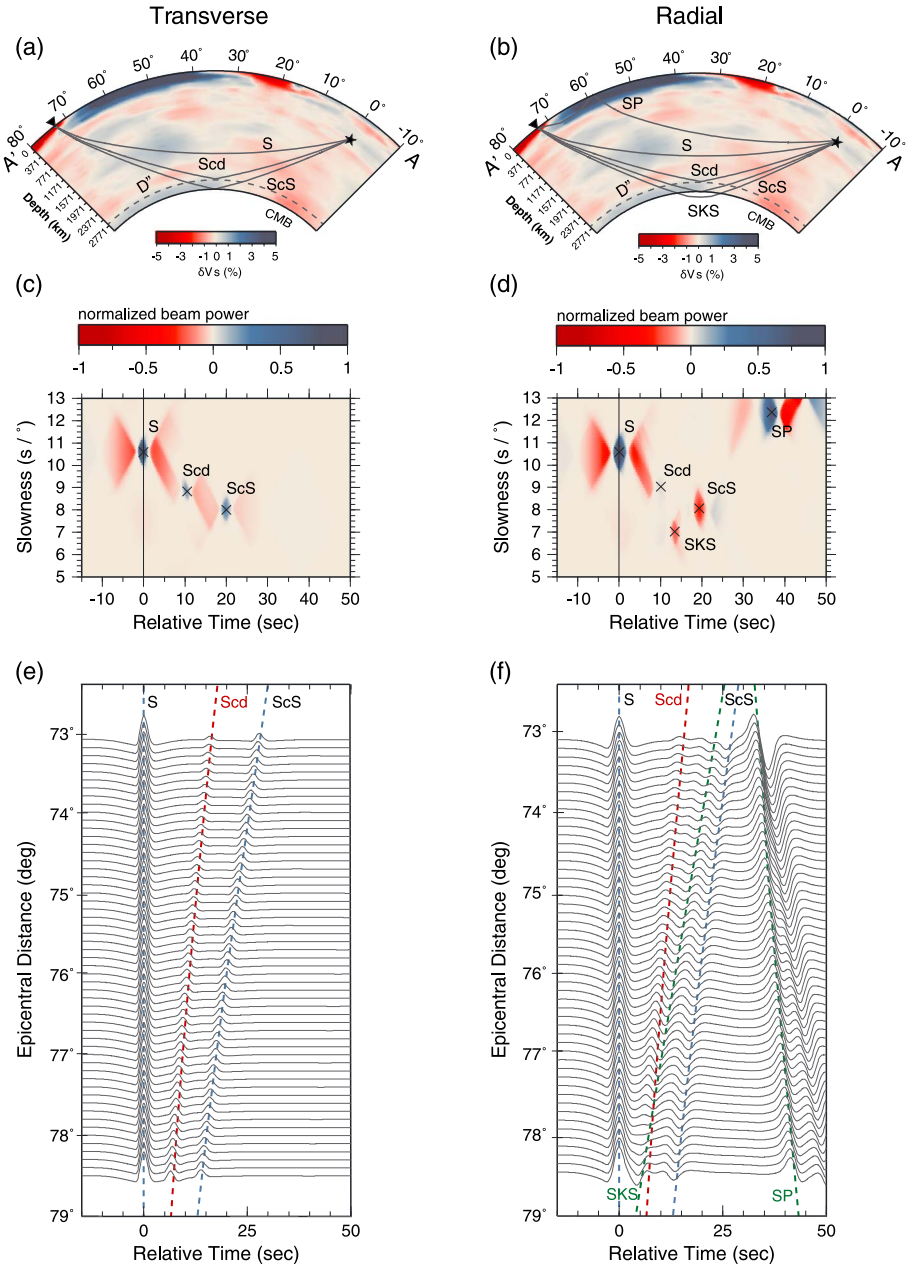

Figure 2. Raypaths observed in our study on top of a cross section through *S* wave tomography model TXBW from event to station (AA′ in Figure 1a) of (a) the transverse component and (b) the radial component. (c, d) Synthetic vespagrams and (e, f) seismic record sections are aligned and normalized to unity on the direct *S* wave, and labeled by the phase names.

presence of the *Scd* arrival, and if it existed, we recorded the differential travel times ($\delta T_{Scd\text{-}S}$ and $\delta T_{ScS\text{-}Scd}$) and differential slownesses ($\delta u_{Scd\text{-}S}$ and $\delta u_{ScS\text{-}Scd}$).

In order to model D″ discontinuity characteristics, we compared data recordings and vespagrams to synthetic seismograms and synthetic vespagrams. We calculated synthetic seismograms using the reflectivity technique [*Fuchs and Müller*, 1971], *SHaxi* [*Jahnke et al.*, 2008] and *PSVaxi* [*Thorne et al.*, 2013] methods. We generated synthetic seismograms based on three types of models which varied in the structure of their velocity profiles (Figure S1 in the supporting information) using the Preliminary Reference Earth Model (PREM) as the background [*Dziewonski and Anderson*, 1981]. In total, we computed synthetic seismograms for 58 unique models and the set of models are shown in Table S1. We used a sharp velocity contrast at

the top of the discontinuity in our models, as gradational boundaries with thicknesses less than 100 km do not strongly affect our results (Figure S2).

We applied the same vespa process to each of the synthetic traces as performed on the data traces. We picked the same differential travel times and slownesses from the synthetic vespagrams as with the data. In order to determine the velocity profile of the D″ discontinuity, we compared data and synthetic predictions by minimizing the travel time and slowness misfits based on the following equations:

$$\delta T = \sqrt{\left(\frac{\delta T^{\text{synth}}_{Scd-S} - \delta T^{\text{obs}}_{Scd-S}}{\delta T^{\text{obs}}_{Scd-S}}\right)^2 + \left(\frac{\delta T^{\text{synth}}_{ScS-Scd} - \delta T^{\text{obs}}_{ScS-Scd}}{\delta T^{\text{obs}}_{ScS-Scd}}\right)^2} \quad (1)$$

$$\delta u = \sqrt{\left(\frac{\delta u^{\text{synth}}_{Scd-S} - \delta u^{\text{obs}}_{Scd-S}}{\delta u^{\text{obs}}_{Scd-S}}\right)^2 + \left(\frac{\delta u^{\text{synth}}_{ScS-Scd} - \delta u^{\text{obs}}_{ScS-Scd}}{\delta u^{\text{obs}}_{ScS-Scd}}\right)^2} \quad (2)$$

where δT and δu are the travel time and slowness misfits, respectively. We applied equal weights to both the travel time and slowness misfit, and calculated the final misfit as

$$\text{Misfit} = \frac{\delta T + \delta u}{2} \quad (3)$$

Midmantle seismic wave speed heterogeneity could bias our results if we do not have stable *ScS-S* differential travel times across our study region. We computed synthetics for cross-sections through tomography model TXBW [*Grand*, 2002] and found small travel time variations (0.54 s average) across our study area. Thus, we do not perform tomography based travel time corrections to these data (Figures S3–S5).

3. Results

Scd arrivals were identified on 20 of the 31 transverse component vespagrams. The remaining 11 vespagrams did not show evidence of an *Scd* arrival. Of the 20 vespagrams where we positively identified *Scd* arrivals, we further categorized these observations as either good cases (12) or borderline cases (8). We ranked the vespagram as good if the *Scd* arrival was clearly present and had a larger amplitude than the background noise, and the energy of the *Scd* arrival was relatively concentrated (the slowness resolution is ≤ 5 s/°). Otherwise, if the potential *Scd* arrival had an amplitude similar to the background noise, and/or the slowness resolution was > 5 s/°, we ranked it as a borderline case. The locations of the central *ScS* bounce points on the CMB for each bin based on the characterization of good-, borderline-, or no-*Scd* arrival are shown in Figures 1a and 1b. We were unable to clearly identify an *Scd* arrival on any of the radial component vespagrams.

Figures 3a–3d shows example vespagrams and record sections for both the transverse and radial components of a good case. We see a clear *Scd* arrival located in between the *S* and *ScS* arrivals on both vespagram and record section of the transverse component, while no *Scd* arrival is definitively observed on the radial component. Nonetheless, there is some smearing of the *SKS* arrival on the radial component vespagram that may interfere with a possible *Scd* arrival. Thus, we cannot rule out an *Scd* arrival in this case.

In order to estimate the velocity profile of the D″ discontinuity, we computed synthetic vespagrams and calculated the misfit between observations and synthetics (Figure S6). Different synthetic model types that share the same discontinuity thickness naturally form into clusters sharing similar misfits (Figures S7–S8), suggesting that the model misfits are more sensitive to the depth variation of the D″ discontinuity than model type or magnitude of the *S* wave velocity increase at the top of the discontinuity, which is also demonstrated in *Wallace and Thomas* [2005]. Our results indicate a D″ discontinuity located 225 to 350 km above the CMB with an average height of 304 ± 14 km ($\sigma = 48$ km) above the CMB. The *S* wave velocity contrast is more difficult to constrain, but our results are consistent with a +2% to +4% velocity increase at the top of the discontinuity. We obtain best fits for models that have a negative velocity gradient starting 200 km above the discontinuity and a negative velocity gradient below the discontinuity that ends at 1.0% above PREM at the CMB. Synthetic seismograms for the best fit model (model 57, velocity profile shown in Figure S9) for bin I06 are shown in Figures 3b and 3d, and demonstrate the high coherence between the predictions and observations. The slightly lower amplitudes of *Scd* and *ScS* arrivals in synthetics are due to the fixed radiation pattern in the *SHaxi* and *PSVaxi* algorithms. The increase in *S* wave velocity at the top of

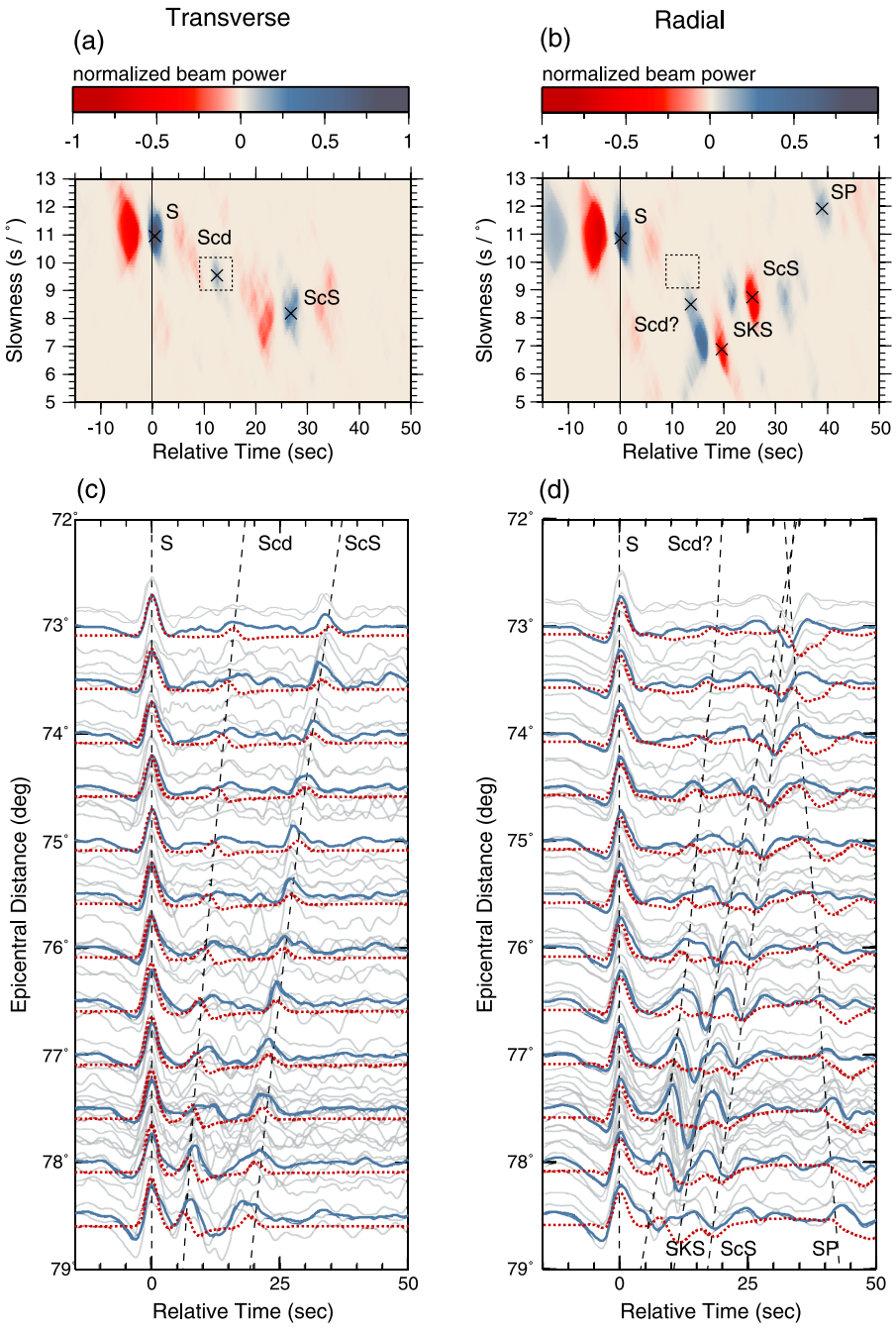

Figure 3. Example vespagrams and record sections of the (a, c) transverse component and (b, d) radial component of BINI06 in Figure 1b. Seismic traces were stacked per 0.5° (blue lines) and labeled with phase names. The stacked transverse and radial synthetic seismograms of best fit model (model 57) of this bin were plotted as dashed red lines in Figures 3c and 3d for comparison. This model has no density change, and we applied an additional +1.5% *P* wave velocity increase to generate radial synthetic seismograms.

the discontinuity is consistent with global observations, and the negative velocity gradients above and below the D″ discontinuity have been suggested by multiple previous studies [e.g., *Wysession et al.*, 1998; *Wallace and Thomas*, 2005]. The observed discontinuity height varies on sub-Fresnel zone (Fresnel zone radius is approximately between 5° and 10°) length scales which has also been noted in previous studies [*Kendall and Shearer*, 1994]. In our study, the negative velocity gradient above the discontinuity is necessary to provide the proper *Scd* travel time delay while still matching the *Scd* slowness.

The 12 good observations can be grouped into two clusters based on their spatial locations. Cluster A is centered at 54°N, 50°W with five bins (F01, F02, F03, G02, and G03), and cluster B is centered at 47°N, 42°W with seven bins (H06, I05, I06, I07, J05, J06, and J07) (Figure 1b). The observations in cluster A are concentrated in a small, ~2° × 2° region, while the observations in cluster B cover a larger 5° × 5° area. The velocity increases at the top of the discontinuity for both clusters are identical, ranging from +2% to +4%. Our discontinuity height estimates also suggest that the depth distribution is similar in cluster A ($\sigma = 45$ km) and cluster B ($\sigma = 52$ km). In cluster A, the height estimation from the five bins shows that the D″ discontinuity is likely located 275 to 325 km above the CMB with an average height of 295 ± 20 km. Only the observation at bin F03 shows a much deeper depth (225 km) of the discontinuity, yet it should be noted that this bin has relatively poor slowness resolution. If we were to remove bin F03 from the calculation, the average height increases to 312 km for cluster A. In cluster B, the height estimations of the northeastern bins (I05, I06, H06, J05, and J06) are similar to the bins in cluster A, ranging from 325 to 350 km with a slightly greater average of 340 ± 6 km, while the depth to the D″ discontinuity trends deeper to the southwest. The height estimations of the bin I07 and J07 located at the southwestern corner of the cluster B shows the D″ discontinuity located 225 to 250 km above the CMB (Table S2). Our combined average of discontinuity height for cluster B is 310 ± 20 km.

The majority of our nonobservations are concentrated at the east edge of our study region (Figure 1b). In cluster A, the locations of the borderline cases fill in the gap between the good observation and nonobservation cases, with a thinner average height of 231 ± 28 km compared with good cases (295 ± 20 km). While in cluster B, the borderline cases have an average height of 250 ± 58 km as well but are located at the west boundary of our study area. The geographic correlation among the different types of observations (good observation, borderline observation, or nonobservation) may be explained by either (1) differences in source-receiver distance of the observations or (2) relationship to lower mantle structure. We explore these possibilities in the next section.

4. Discussion and Conclusions

No clear *Scd* arrivals were observed on these radial component data. Constructive and destructive interference effects from the *SKS* arrival may mask possible *Scd* arrivals, but previous studies have also speculated that transverse isotropy in the D″ layer may explain the lack of *Scd* observations on the radial component [e.g., *Matzel et al.,* 1996]. *Scd* arrivals on the radial component data may be present but it is difficult to confirm. There is a possible positive amplitude arrival that merges with the *SKS* leading downswing (Figure 3d). This arrival also appears separate from *SKS* on the vespagram (Figure 3b). However, if this is *Scd* on the radial component, it arrives with slightly later arrival time and smaller slowness than *Scd* on the transverse component. A later *Scd* arrival on the radial component is consistent with anisotropy in post-perovskite where *SH* waves are predicted to be faster than *SV* waves [*Miyagi et al.,* 2010]. One previous study has demonstrated weak, or no anisotropy immediately south of our study area [*Garnero et al.,* 2004]. But increased strain possibly induced by the subducting Farallon plate, as discussed below, could locally increase anisotropy in our study region which will be heavily dependent on lower mantle flow direction [e.g., *Moore et al.,* 2004; *Thomas et al.,* 2011].

Our estimate of D″ discontinuity height above the CMB (average = 304 ± 14 km, ranging from ~225 to 350 km) is similar but slightly greater to estimates from previous studies in the surrounding region (ranging from ~200 to 286 km; Figure 1a). Our study area is located in a region where ancient subduction of the Farallon plate has been inferred [e.g., *Bunge and Grand*, 2000; *Conrad et al.,* 2004]. Previous *S* wave tomography studies [e.g., *Mégnin and Romanowicz*, 2000; *Grand*, 2002; *Simmons et al.,* 2010; *Ritsema et al.,* 2011] also show that our study area is located at a boundary between fast and slow velocity regions at the CMB (Figure 1b), which could be the boundary between ancient Farallon plate and normal mantle. Therefore, the cold downwelling mantle, combined with an increase in mid-ocean ridge basalt composition of the Farallon plate, could cause the discontinuity beneath our study region to occur at a greater height above the CMB [e.g., *Grocholski et al.,* 2012]. For cluster A, both our good and borderline observations are located within the fast *S* wave velocity region, while most of our nonobservations are concentrated at the eastern edge of our study region closest to the slow *S* wave velocities. Hence, our observations may be consistent with sampling the easternmost edge of the ancient Farallon plate.

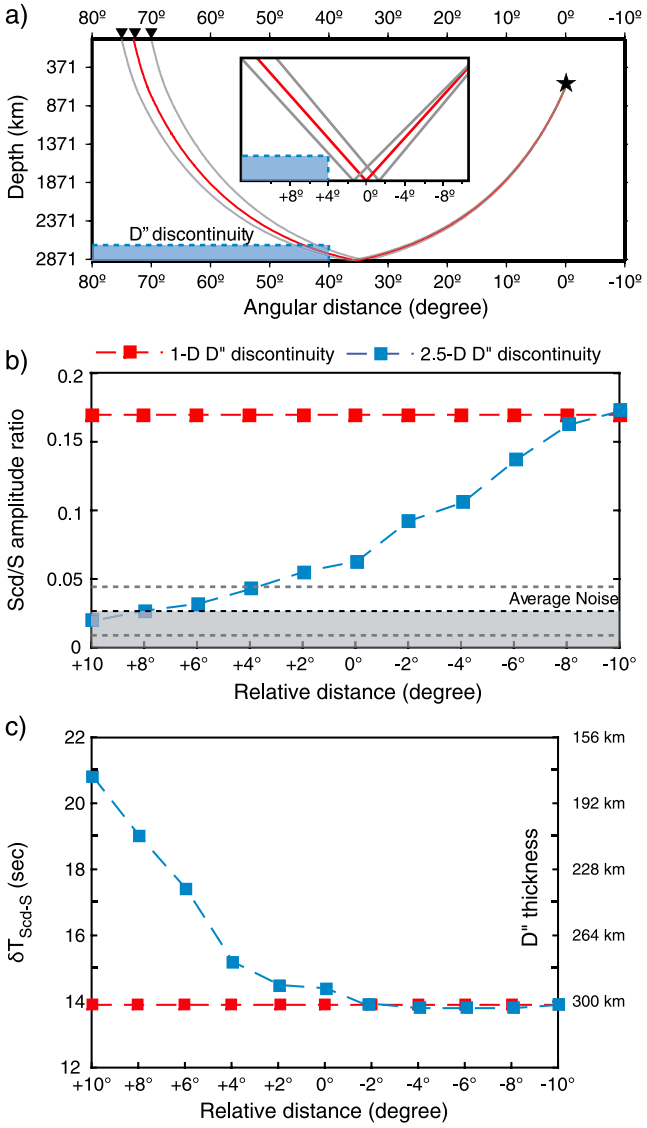

Figure 4. (a) Sketch of the 2.5-D D″ discontinuity model with a sharp edge. The inset shows detail near the CMB and plots angular distance of the edge of the fast anomaly relative to the *ScS* CMB bounce point for an epicentral distance of 73°. (b) The *Scd/S* amplitude ratio with respect to the relative distance from the edge of the fast anomaly. Observed noise is plotted as average noise level (black dashed line) and standard deviation (grey dashed line). (c) Travel time difference between *Scd* and *S* of the 1-D (red) and 2.5-D (blue) models as a function of relative distance from the edge of the fast anomaly. D″ height estimates based on $\delta T_{Scd\text{-}S}$ are shown on the right-hand *y* axis right.

Yet our observations are potentially biased due to source-receiver epicentral distance. In general, the amplitude of the *Scd* arrival decreases with decreasing epicentral distance, which may lead to decreased detectability of the *Scd* arrivals. The epicentral distance range for our nonobservations ($\Delta = 64°–73°$), borderline observations ($\Delta = 68°–74°$), and good observations ($\Delta = 70°–76°$) for cluster A tends to increase. The predicted *Scd/S* amplitude ratio for a 1-D D″ discontinuity model 300 km above the CMB with an *S* wave velocity contrast of +2% ranges from (1) 0.0662–0.1078 for epicentral distances where we have nonobservations, (2) 0.1078–0.1697 for the borderline observation distances, and (3) 0.1697–0.2132 for the good observation distances. These amplitude ratios are well above the average noise level (0.027) in our vespagrams. Thus, if the D″ discontinuity extends laterally throughout our study region, we should be able to observe the *Scd* arrivals on vespagrams. Yet because there is a relationship between epicentral distance and *Scd/S* amplitude ratio, we cannot rule out the possibility that our nonobservations are solely due to decreased ability to detect the *Scd* arrival for these bins. But we note that there is overlap in the epicentral distance range of nonobservations and borderline observations which suggests our nonobservations may be related to lower mantle structural effects.

The other possibility is that the D″ discontinuity terminates near the eastern boundary of our study region. In order to assess this possibility, we computed synthetic seismograms for a series of 2.5-D models with a sharp eastern boundary on the D″ discontinuity. The synthetics were computed for a discontinuity located 300 km above the CMB with a 2% *S* wave velocity increase. For comparison, results for a 1-D continuous D″ discontinuity model at the same height with the same velocity contrast are also shown in Figures 4a and 4b. We fixed the distance between the source and the center of the receiver array at 73° so that the *ScS* raypaths are centered at 35°. We allowed the position of the discontinuity edge to vary in angular distance from the source between 25° and 45° in 2° increments (±10° from the central *ScS* bounce point; Figure 4a). We observe two important effects. First, as the edge position moves closer to the receiver array, the *Scd/S* amplitude ratio decreases (Figure S10). When the edge reaches a position of +8° from the central *ScS* bounce point, the *Scd/S* amplitude ratio has decayed to 0.026, which is below the

average noise level (0.027) of our best data and would thus no longer be observable (Figure 4b). Even for an edge position of +4°, the *Scd/S* amplitude ratio has dropped enough to be within the range of noise observed in this study. This result suggests that the discontinuity edge can be located as far as +4° to +8° away (closer to the receivers) from the central *ScS* bounce point of the observations and still be detectable; yet if the edge is located greater than +4° from the boundary, detectability will be challenging. Second, as the edge position increases this causes measurements of $\delta T_{Scd\text{-}S}$ to increase. This results in a decrease of our discontinuity height estimate (Figure 4c). For example, moving the edge position to +4° from the central *ScS* bounce points causes an increase in $\delta T_{Scd\text{-}S}$ of 1.3 s, which in turn results in a decreased estimate of discontinuity height of roughly 20 km.

These two effects can be used to estimate the location of the discontinuity edge if it exists. For cluster A, the borderline cases are roughly located 2° to the east of the good cases and 3° west of the nonobservations (Figure 1b). They were previously not included in our average estimates of D″ discontinuity structure because of their questionable *Scd* arrivals with low amplitudes and poor slowness resolution. However, these characteristics are consistent with our synthetic predictions for a D″ discontinuity model with a sharp edge. If the edge is located ~2° to 4° west of the central bounce point of the good cases, the *Scd* arrivals are still detectable for good and borderline observations (Figure S11). Additionally, the average height difference (64 km) of the D″ discontinuity between the good (295 ± 20 km) and borderline cases (231 ± 28 km) suggests that the edge should be located ~4° to 6° west of the central bounce point of the borderline cases. There is not a general pattern between the good and borderline observations in cluster B. We also tested models where the boundary edge has a shallower slope (Figure S12). Our results are consistent with a boundary that has a slope as shallow as 30°, yet *Scd* amplitude considerations suggest the boundary is nearer to vertical (Figure S13). These synthetic analyses of a D″ discontinuity with a sharp boundary suggest that the D″ discontinuity may not extend across the North Atlantic Ocean, rather terminates abruptly between 45° and 50° W longitudes, which corresponds to the inferred position of the easternmost edge of the subducted Farallon plate.

Acknowledgments

We gratefully acknowledge the University of Utah Center for High Performance Computing (CHPC) for computer resources and support. M.T. and Y.Y. were partially supported by NSF grant EAR-1014749. Figures were drawn using the Generic Mapping Tools [*Wessel and Smith*, 1998]. Data used in this study may be downloaded from http://web.utah.edu/thorne/pubs.html. We thank two anonymous reviewers for constructive review and suggestions.

The Editor thanks two anonymous reviewers for their assistance in evaluating this paper.

References

Braña, L., and G. Helffrich (2004), A scattering region near the core-mantle boundary under the North Atlantic, *Geophys. J. Int.*, *158*(2), 625–636, doi:10.1111/j.1365-246X.2004.02306.x.

Bunge, H., and S. Grand (2000), Mesozoic plate-motion history below the northeast Pacific Ocean from seismic images of the subducted Farallon slab, *Nature*, *405*, 337–340.

Cobden, L., and C. Thomas (2013), The origin of D″ reflections: A systematic study of seismic array data sets, *Geophys. J. Int.*, *194*(2), 1091–1118, doi:10.1093/gji/ggt152.

Conrad, C. P., C. Lithgow-Bertelloni, and K. E. Louden (2004), Iceland, the Farallon slab, and dynamic topography of the North Atlantic, *Geology*, *32*(3), 177, doi:10.1130/G20137.1.

Crotwell, H. P., T. J. Owens, and J. Ritsema (1999), The TauP Toolkit: Flexible seismic travel-time and ray-path utilities, *Seismol. Res. Lett.*, *70*(2), 154–160, doi:10.1785/gssrl.70.2.154.

Dziewonski, A. M., and D. L. Anderson (1981), Preliminary reference Earth model, *Phys. Earth Planet. Inter.*, *25*(4), 297–356, doi:10.1016/0031-9201(81)90046-7.

Fuchs, K., and G. Müller (1971), Computation of synthetic seismograms with the reflectivity method and comparison with observations, *Geophys. J. R. Astron. Soc.*, *23*(4), 417–433, doi:10.1111/j.1365-246X.1971.tb01834.x.

Garnero, E. J., M. M. Moore, T. Lay, and M. J. Fouch (2004), Isotropy or weak vertical transverse isotropy in D″ beneath the Atlantic Ocean, *J. Geophys. Res.*, *109*, B08308, doi:10.1029/2004JB003004.

Grand, S. P. (2002), Mantle shear-wave tomography and the fate of subducted slabs, *Philos. Trans. R. Soc. London, Ser. A*, *360*(1800), 2475–2491.

Grocholski, B., K. Catalli, S.-H. Shim, and V. Prakapenka (2012), Mineralogical effects on the detectability of the postperovskite boundary, *Proc. Natl. Acad. Sci. U.S.A.*, *109*(7), 2275–2279, doi:10.1073/pnas.1109204109.

Houard, S., and H.-C. Nataf (1992), Further evidence for the "Lay discontinuity" beneath northern Siberia and the North Atlantic from short-period P-waves recorded in France, *Phys. Earth Planet. Inter.*, *72*(3–4), 264–275, doi:10.1016/0031-9201(92)90206-B.

Jahnke, G., M. S. Thorne, A. Cochard, and H. Igel (2008), Global SH-wave propagation using a parallel axisymmetric spherical finite-difference scheme: Application to whole mantle scattering, *Geophys. J. Int.*, *173*(3), 815–826.

Kendall, J.-M., and P. M. Shearer (1994), Lateral variations in D″ thickness from long-period shear wave data, *J. Geophys. Res.*, *99*, 11,575–11,590, doi:10.1029/94JB00236.

Krüger, F., M. Weber, F. Scherbaum, and J. Schlittenhardt (1995), Evidence for normal and inhomogeneous lowermost mantle and core-mantle boundary structure under the Arctic and northern Canada, *Geophys. J. Int.*, *122*(122), 637–657.

Matzel, E., M. K. Sen, and S. P. Grand (1996), Evidence for anisotropy in the deep mantle beneath Alaska, *Geophys. Res. Lett.*, *23*, 2417–2420, doi:10.1029/96GL02186.

Mégnin, C., and B. Romanowicz (2000), The three-dimensional shear velocity structure of the mantle from the inversion of body, surface and higher-mode waveforms, *Geophys. J. Int.*, *143*(3), 709–728, doi:10.1046/j.1365-246X.2000.00298.x.

Miyagi, L., W. Kanitpanyacharoen, P. Kaercher, K. K. M. Lee, and H.-R. Wenk (2010), Slip systems in MgSiO3 post-perovskite: Implications for D″ anisotropy, *Science*, *329*(5999), 1639–1641, doi:10.1126/science.1192465.

Moore, M. M., E. J. Garnero, T. Lay, and Q. Williams (2004), Shear wave splitting and waveform complexity for lowermost mantle structures with low-velocity lamellae and transverse isotropy, *J. Geophys. Res.*, *109*, B02319, doi:10.1029/2003JB002546.

Murakami, M., K. Hirose, K. Kawamura, N. Sata, and Y. Ohishi (2004), Post-perovskite phase transition in MgSiO3, *Science*, *304*(5672), 855–858, doi:10.1126/science.1095932.

Oganov, A. R., and S. Ono (2004), Theoretical and experimental evidence for a post-perovskite phase of MgSiO3 in Earth's D″ layer, *Nature*, *430*(6998), 445–448, doi:10.1038/nature02701.

Ritsema, J., A. Deuss, H. J. van Heijst, and J. H. Woodhouse (2011), S40RTS: A degree-40 shear-velocity model for the mantle from new Rayleigh wave dispersion, teleseismic traveltime and normal-mode splitting function measurements, *Geophys. J. Int.*, *184*(3), 1223–1236, doi:10.1111/j.1365-246X.2010.04884.x.

Rost, S., and C. Thomas (2009), Improving seismic resolution through array processing techniques, *Surv. Geophys.*, *30*(4–5), 271–299, doi:10.1007/s10712-009-9070-6.

Simmons, N. A., A. M. Forte, L. Boschi, and S. P. Grand (2010), GyPSuM: A joint tomographic model of mantle density and seismic wave speeds, *J. Geophys. Res.*, *115*, B12310, doi:10.1029/2010JB007631.

Thomas, C., J. Wookey, J. Brodholt, and T. Fieseler (2011), Anisotropy as cause for polarity reversals of D″ reflections, *Earth Planet. Sci. Lett.*, *307*(3–4), 369–376, doi:10.1016/j.epsl.2011.05.011.

Thorne, M. S., E. J. Garnero, G. Jahnke, H. Igel, and A. K. McNamara (2013), Mega ultra low velocity zone and mantle flow, *Earth Planet. Sci. Lett.*, *364*, 59–67, doi:10.1016/j.epsl.2012.12.034.

Wallace, M., and C. Thomas (2005), Investigating D″ structure beneath the North Atlantic, *Phys. Earth Planet. Inter.*, *151*(1–2), 115–127, doi:10.1016/j.pepi.2005.02.001.

Weber, M., and M. Körnig (1992), A search for anomalies in the lowermost mantle using seismic bulletins, *Phys. Earth Planet. Inter.*, *73*(1–2), 1–28, doi:10.1016/0031-9201(92)90104-4.

Wessel, P., and W. H. F. Smith (1998), New, improved version of Generic Mapping Tools released, *Eos Trans. AGU*, *79*(47), 579, doi:10.1029/98EO00426.

Wysession, M. E., T. Lay, J. Revenaugh, Q. Williams, E. J. Garnero, R. Jeanloz, and L. H. Kellogg (1998), The D″ discontinuity and its implications, in *The Core-Mantle Boundary Region*, edited by M. Gurnis et al., pp. 273–297, AGU, Washington, D. C.